The Astronomical Journal, 130:1337–1344, 2005 October

THE EVOLUTION OF STELLAR MASS IN GALAXIES IN THE NICMOS ULTRA DEEP FIELD

S. D. J. Gwyn[1] and F. D. A. Hartwick
Department of Physics and Astronomy, University of Victoria, P.O. Box 3055, STN CSC, Victoria, BC V8W 3P6, Canada; gwyn@uvic.ca
Received 2005 March 10; accepted 2005 June 19

ABSTRACT

We measure the buildup of the stellar mass of galaxies from $z = 6$ down to $z = 1$. Using 15 band multicolor imaging data in the NICMOS Ultra Deep Field we derive photometric redshifts and masses for 796 galaxies down to $H_{AB} = 26.5$ mag. The derived evolution of the global stellar mass density of galaxies is consistent with previous star formation rate density measurements over the observed range of redshifts. Beyond the observed range, maintaining consistency between the global stellar mass and the observed star formation rate suggests the epoch of galaxy formation was $z = 16$.

Key words: galaxies: evolution — galaxies: high-redshift — galaxies: luminosity function, mass function — galaxies: stellar content

1. INTRODUCTION

For the last 10 years, the Lilly-Madau diagram (Lilly et al. 1996; Madau et al. 1996, 1998) has been central to the discussion of galaxy evolution. It shows that the star formation rate density (SFRD) increases with redshift to $z \sim 1$ and decreases beyond that. In the last year, thanks to the Ultra Deep Field (UDF), several points have been added at the high-redshift end of the diagram (Bouwens et al. 2004a, 2004b; Bunker et al. 2004; Stanway et al. 2004).

While the Lilly-Madau diagram is a useful tool for studying galaxy evolution, it is subject to some uncertainties, particularly at the high-redshift end. Typically, high-redshift galaxies are selected with the Lyman break method, the UV luminosity function is computed, and this is then extrapolated out to the faint end and integrated. UV light is a good tracer of star formation, so multiplying the total UV luminosity density by a conversion factor yields the SFRD. One source of uncertainty lies in identifying the high-redshift galaxies: the Balmer break may be confused with the Lyman break, putting spurious galaxies *in* the sample, and galaxies with heavy extinction may be left *out*. Extinction must also be considered when converting the UV flux into a star formation rate. Typically, a factor of 5 is used for the extinction correction, but the exact value is imperfectly known. For these reasons, it would be satisfying to have some corroboration of the star formation rate.

The SFRD is essentially dM_*/dt, where M_* is the baryonic mass in the form of stars, normalized to 1 Mpc^3. The integral of dM_*/dt is just $M_*(t)$, the global stellar mass density (GSMD). Deep infrared images and some means of determining redshift (either photometrically or spectroscopically) are required to measure the GSMD.

The NICMOS UDF is ideal for this purpose. It has deep infrared imaging (26.5 AB magnitude) as well as a wealth of imaging in other bands with which to compute photometric redshifts. The wavelength coverage extends from U to K in 15 overlapping bands from a number of different surveys. This paper describes measurements of GSMD out to $z = 6$ in the NICMOS UDF.

There are a number of measurements of the GSMD in the literature. Rudnick et al. (2003), working with the Hubble Deep Field–South (HDF-South) and the FIRES K data (Labbé et al. 2003), measured the rest-frame optical properties of galaxies out to $z = 3$ and from their average properties deduced their masses. Dickinson et al. (2003) used the HDF-North with NICMOS J and H observations. They computed the global luminosity density out to $z = 3$, computed the average mass-to-light ratio of galaxies at these redshifts, and so deduced the global mass. Fontana et al. (2004), on the other hand, computed stellar masses for galaxies individually. They used the K20 survey, which consists of *UBVRIzJK* observations with a limiting magnitude of $K_{Vega} = 20$ and spectroscopic redshifts, out to $z = 2$. Glazebrook et al. (2004) used the Gemini Deep Deep Survey (GDDS; Abraham et al. 2004), which is also based on multiwavelength data and spectroscopic redshifts but extends slightly deeper and is specially tuned to the wavelength range $0.8 < z < 2$. Drory et al. (2004) used the Munich Near-Infrared Cluster Survey (MUNICS; Drory et al. 2001), which is shallower ($K_{Vega} = 19.5$) and extends only out to $z = 1.4$. The highest redshift survey so far is that of Drory et al. (2005), who used the Great Observatories Origins Deep Survey–South (GOODS-South) data and FORS Deep Field (Heidt et al. 2003) to go to $z = 5$ and $K_{AB} = 25.4$ mag.

In § 2 we describe how we resampled all the various imaging data and produced the catalog of photometry and photometric redshifts. In § 3 we derive masses and mass functions for the galaxies in the sample and examine the evolution of the GSMD with time. In § 4 we compare our measurements of the GSMD evolution with the Hartwick (2004) model, the predictions from the SFRD, and previous work. Throughout this paper we use the AB magnitude system (Oke 1974) and adopt the concordance cosmology of $H_0 = 70\,\mathrm{km\,s^{-1}\,Mpc^{-1}}$, $\Omega_m = 0.3$, and $\Omega_\Lambda = 0.7$.

2. DATA

2.1. *Data Sources*

The NICMOS UDF field lies within the GOODS-South region of the sky and has been imaged by a large number of telescopes at a variety of wavelengths. For this project four sources of imaging data for this field were considered.

Space-based infrared imaging—These data were taken with NICMOS under the *Hubble Space Telescope* (*HST*) Cycle 12 Treasury Program and forms the basis for this work. It was taken

[1] Guest User, Canadian Astronomy Data Centre, which is operated by the Herzberg Institute of Astrophysics, National Research Council of Canada.

in two bands, F110W and F160W, which roughly correspond to J and H.[2]

Space-based optical imaging—This is the UDF proper. The data were taken in four bands: F435W (B), F606W (somewhere between V and R), F775W (I), and F850LP (Z).[3]

Ground-based infrared imaging—These images were taken as part of the GOODS survey with ISAAC on the VLT (B. Vandame 2005, in preparation). There are three bands: JHK'. Unlike the other data sets, the ISAAC data has been released as one image per pointing with multiple pointings, rather than a combined mosaic.[4]

Ground-based optical imaging—These were taken as part of the ESO Imaging Survey (EIS; Arnouts et al. 2001). There are six bands: $U'UBVRI$ (U' is slightly bluer than U).[5]

All of these data have been released in fully processed form. No additional processing is necessary. However, the images in each data set have different scales and sizes than the images in other data sets.

2.2. *Resampling the Images*

There are two drivers to the photometry: in order to compute photometric redshifts, it is necessary to have accurate colors. For this, fixed circular aperture photometry, preferably through a small aperture, is sufficient. The photometry is also used for computing masses of the galaxies; for this, accurate total magnitudes are necessary. Total magnitudes are best measured through an adaptive elliptical aperture (Kron 1980). If there are to be no systematic shifts, then these apertures must be matched in all bands. If the images are registered, this can be done easily using SExtractor (Bertin & Arnouts 1996) in "double-image mode." Since all the images have different scales, they must be resampled to put them on the same astrometric grid.

The resampling was done with SWarp.[6] SWarp's main purpose is to combine several (not necessarily overlapping) images into a single image. It resamples the input images to put them on a common astrometric grid and scales the flux to correct for any photometric shifts between the images. It can also be used to just remap a single image with no flux scaling.

The NICMOS H image was used as the base image to which all the other images were matched. The NICMOS J image needed no remapping, as it was already on the same scale. The optical images from the UDF were remapped. This changed their scale from $0\farcs03$ to $0\farcs09$ pixel^{-1}, making them slightly undersampled. The ISAAC images were SWarped together so that different pointings in each band were combined into a single mosaic. The EIS images show a small but systematic shift in astrometry with respect to the other data set. Since this shift is several times smaller than the seeing of the ground-based EIS images, it was noted but not corrected. Both sets of ground-based images are greatly oversampled by the remapping.

The resampling does not introduce any appreciable shifts in either position or flux. The SWarp documentation claims that with 3 pixel Lanczos interpolation, position is conserved to within 0.1 pixel and flux is conserved to 0.2%. We checked this by comparing the properties of objects in the original images to the same properties in the resampled images. Position was measured by centroid and flux by magnitude in a $1''$ diameter aperture. No significant shifts in either position or flux were noted.

2.3. *Photometry*

SExtractor (Bertin & Arnouts 1996) was run in double-image mode on all the images in all the bands. The NICMOS F160W (H band) image was used as the reference image: the objects were detected in H, and Kron (1980) style variable elliptical apertures (*mag_auto* in SExtractor) were computed using the surface brightness profile of the galaxies in the H band. Identical apertures were then used to measure photometry in the other images.

Initially, we used the photometric zero points given by the producers of each image. However, it soon became apparent that these zero points were in slight systematic disagreement with each another. This was discovered by converting all the magnitudes for different objects into fluxes and plotting these fluxes as a function of central wavelength of the filter in question. There are a total of 15 overlapping photometric bands covering the wavelength range 3500–21500 Å. Therefore, the spectral energy distributions (SEDs) generated in this manner are very well defined. It was found that some bands were systematically higher relative to neighboring bands. To derive the values of the photometric offsets, we selected the 39 galaxies in the NICMOS UDF with published redshifts. We fitted the SEDs of these galaxies with template spectra, using a similar method as the photometric redshift technique described in § 2.4 but with the redshift fixed to the published spectroscopic redshift. Again, systematic offsets were noted between the templates and the measured SEDs. These offsets were not correlated with wavelength but were instead correlated with the source of the images. This indicates that the problem lies not with the templates but with the photometry. For example, the difference in image quality between the low-resolution ground-based data and high-resolution space-based data will cause light to be systematically scattered out of an aperture chosen from the space-based image. Rather than delve into the details of the origins of the shifts, we took a pragmatic approach and applied the average shift determined from the 39 galaxies. The zero-point shifts determined in this manner are small, typically 0.1 mag.

We investigated the completeness limits in terms of total magnitude and peak surface brightness of the photometry. This was done by adding artificial galaxies at random locations in the image and then rerunning SExtractor to find what fraction of the galaxies could be recovered. Rather than use completely artificial galaxies, several bright, isolated galaxies were identified in the image. Small image sections (thumbnails) around these galaxies were extracted. The thumbnails were then modified by:

Scaling the flux levels—This consists of multiplying the value of each pixel by a factor. This changes both the total magnitude and the peak surface brightness simultaneously.

Resampling the images—This means spreading the light from a galaxy over more pixels or concentrating it into fewer pixels. It was done with bilinear interpolation, rather than the more sophisticated Lanzcos interpolation used by SWarp. This leaves the total magnitude intact (as there is no change in flux) but changes the peak surface brightness.

By a combination of these two modifications, one can artificially fade images of galaxies of arbitrary total magnitude and peak surface brightness. The galaxies were chosen to be sufficiently bright such that the sky noise from the thumbnail after being faded was negligible relative to the sky noise from the

[2] Data available at ftp://archive.stsci.edu/pub/hlsp/udf/nicmos-treasury/.

[3] Data available at ftp://archive.stsci.edu/pub/hlsp/udf/acs-wfc/.

[4] Data available at http://www.eso.org/science/eis/old_eis/eis_rel/goods/goods_rel_isaac.html.

[5] Data available at http://www.eso.org/science/eis/old_eis/eis_rel/goods/goods_rel_other.html.

[6] The documentation for SWarp is available at http://terapix.iap.fr/rubrique.php?id_rubrique=49.

image section to which the thumbnail was added. The 90% completeness limit was found to be $H_{\rm AB} = 26.5$ mag in total magnitude and $\mu_H = 25$ mag arcsec^{-2} in surface brightness.

The false positive limit was tested by multiplying the original H-band image by -1 and running SExtractor as before. SExtractor detects sources by looking for a number of contiguous pixels above a certain flux threshold relative to sky background. In this particular case, the minimum detection area was set to 5 contiguous pixels and the detection threshold was set to 1.5 σ of the background. This means each object found by SExtractor is detected at the 7.5 σ level, assuming all the pixels are uncorrelated. In practice, the drizzling method (Fruchter & Hook 2002) used to construct the F160W image leads to slightly correlated pixels. Multiplying the image by -1 means all the real sources are below the sky level and therefore will not be detected. Any sources that *are* detected by SExtractor in the negative image are noise artifacts, not real objects. Thus, the number of objects detected in the negative image is a good measure of the false positive rate. At $H_{\rm AB} = 26.5$ mag, the false positive rate is just under 8%. The final catalog contains 796 galaxies down to $H_{\rm AB} = 26.5$ mag.

2.4. *Photometric Redshifts*

Photometric redshifts were calculated for all the objects in the field. The usual template-fitting, χ^2 minimization method (Loh & Spillar 1986; Gwyn 2001) was used. The photometric data for each galaxy are converted into SEDs. The magnitude in each bandpass is converted to a flux (power per unit bandwidth per unit aperture area) at the central, or effective, wavelength of the bandpass. When the flux is plotted against wavelength for each of the bandpasses, a low-resolution SED is created.

A set of template spectra of all Hubble types and redshifts ranging from $z = 0$ to 10 is compiled. The redshifted spectra are reduced to the passband-averaged fluxes at the central wavelengths of the passbands, in order to compare the template spectra with the SEDs of the observed galaxies. The basis of the template set are the Coleman et al. (1980) spectra. These are supplemented with the SB2 and SB3 spectra from Kinney et al. (1996). Note that this is the same set of spectra used by Benítez (2000).

All these spectra have been extrapolated slightly into the UV. For the purposes of photometric redshifts, it has been found that the exact nature of this extrapolation is unimportant. The size of the Lyman break imposed on the spectra of high-redshift galaxies by the intergalactic medium (IGM) makes the exact shape of the underlying galaxy spectrum almost irrelevant. To account for the effects of the IGM, we use the prescription of Madau (1995). Having only a small number of templates can cause aliasing in photometric redshifts. Therefore, 10 new templates have been created in between each pair of the six original templates. There are a total of 51 templates.

The SED derived from the observed magnitudes of each object is compared to each template spectrum in turn. The best matching spectrum, and hence the redshift, is determined by minimizing χ^2 as defined by the equation

$$\chi^2(t,z) = \sum_{i=1}^{N_f} \frac{[F_i - \alpha T_i(t,z)]^2}{\sigma_{F_i}^2}, \qquad (1)$$

where t is the spectral type, z is the redshift, N_f is the number of filters, F_i and σ_{F_i} are the flux and the uncertainty in the flux in each bandpass of the observed galaxy, respectively, T_i is the flux in each bandpass of the template being considered, and α is a normalization factor given by

$$\alpha = \frac{\sum_{i=1}^{N_f} \left(F_i T_i / \sigma_{F_i}^2 \right)}{\sum_{i=1}^{N_f} \left(T_i^2 / \sigma_{F_i}^2 \right)}. \qquad (2)$$

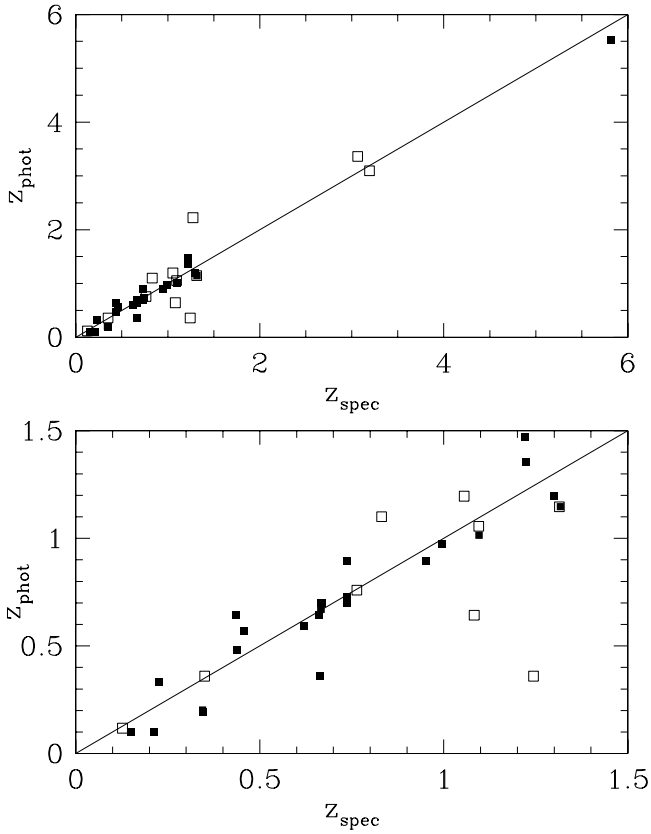

FIG. 1.—Photometric redshifts. The panels show a comparison between the photometric redshifts and spectroscopic redshifts for our sample. The top panel shows the results for all the galaxies with spectroscopic redshifts in the NICMOS UDF. The bottom panel shows the same thing with an expanded scale for $0 < z < 1.5$. The filled points indicate objects with secure redshifts; the open points indicate doubtful identifications.

Figure 1 shows a comparison of the photometric redshifts with the 39 published spectroscopic redshifts. These were taken from the work of Vanzella et al. (2005), Le Fèvre et al. (2004), Szokoly et al. (2004), Croom et al. (2001), Stanway et al. (2004), and Strolger et al. (2004) as compiled by Rettura (2004). The filled points show objects with secure redshifts. The open points show objects for which the spectroscopic redshift identification is less secure for one of a number of reasons. The most common reason is that the "redshift quality flag" given in the relevant paper was low (e.g., quality = 1 or 2 in Le Fèvre et al. 2004). In addition, both objects from the Szokoly et al. (2004) paper are identified as quasars or AGN. Since we do not include such templates in our photometric redshift method, it would be slightly surprising if we could measure accurate photometric redshifts for these objects. In fact, both objects show good agreement but are indicated with open points anyway. Finally, the position of one of the spectroscopic redshift objects lies directly between two objects, which are resolved in the *HST* images. These objects are merged in lower resolution images.

Taking into account only the objects with secure redshifts, the photometric redshift error is $\sigma_z = 0.06(1+z)$ with no catastrophic

failures. Taking into account all the objects increases this to $\sigma_z = 0.12(1+z)$, with two catastrophic failures for 39 objects.

The resampled images and the catalog with photometry and photometric redshifts are available on the Mergers, Morphology, and Mass Buildup Project Web site.[7] Also available at this site are the SWarp and SExtractor configuration files.

3. MASSES

3.1. *Mass Measurements*

We determined masses for each galaxy with a template-fitting process similar to the photometric redshift method described above. The photometry for each galaxy is converted into an SED and compared to a series of templates as before. In this case, the redshift of the templates being considered is held fixed during the χ^2 minimization.

Rather than the empirical Coleman et al. (1980) and Kinney et al. (1996) templates, a selection of the PEGASE 2.0 galaxy spectral evolution models (Fioc & Rocca-Volmerange 1997) were used as templates. The templates were redshifted as before, and the IGM correction of Madau (1995) was applied. Each of these templates was normalized to $M_* = 1\ M_\odot$. Therefore, the stellar mass of each galaxy is given by

$$M_* = \alpha\left(4\pi d_L^2\right), \tag{3}$$

where α is the normalization factor for the best-fitting template described in equation (2) and d_L is the luminosity distance.

The models span the full range of ages from $t = 0$ to 14 Gyr. The metallicity was set to zero (no metals) at $t = 0$ in the models. As each model evolves in time, the metallicity evolves self-consistently. We added extinction to the models using the reddening curve of Calzetti (1997). The amount of extinction was varied from $A(V) = 0$ to 1. The Kroupa et al. (1993) initial mass function (IMF) was used exclusively. The template spectra are essentially degenerate with respect to the IMF.

3.2. *Mass Uncertainties*

While the template-fitting process will select one template as being the best fit, there are several templates that will be consistent with a given set of photometry and its associated uncertainty. Using equation (3) with these alternate templates gives slightly different masses. The range of template masses that are still consistent with the photometry gives an estimate on the random uncertainty on the mass. Here we take all templates that match the photometry such that $\chi^2 < \chi^2_{\rm best} + 1$ (where $\chi^2_{\rm best}$ is the reduced χ^2 of the best-fitting template) to be "consistent." The mean mass uncertainty was found to be 0.15 dex. Mass uncertainty, not surprisingly, was found to be an increasing function of apparent H magnitude. We adopted $\sigma_{\rm mass} = 0.1$ for $H_{\rm AB} < 25$ mag and $\sigma_{\rm mass} = 0.2$ for $H_{\rm AB} > 25$ mag.

A potential source of systematic error is the choice of IMF. We chose the Kroupa et al. (1993) IMF rather than the Salpeter (1955) IMF that is commonly adopted in galactic evolution studies. Switching to a Salpeter IMF causes a systematic shift in the masses of -0.12 dex, in the sense $M_{\rm Kroupa} - M_{\rm Salpeter} = -0.12$ dex. Switching to the Baldry & Glazebrook (2003) IMF also causes a systematic shift of 0.12 dex, but in the other direction.

There are also uncertainties in the mass that are due to the uncertainties in the redshift. A photometric redshift that is higher than the true redshift will cause the measured mass to be artificially higher in addition to any random uncertainties from the template fitting. We deal with these coupled uncertainties in § 3.3.

3.3. *Mass Functions and Total Masses*

We used the $1/V_a$ method to compute mass functions in a series of redshift bins. For each galaxy we measure the accessible volume, V_a, which is the volume the galaxy *could* be in and still be visible in the survey. The sides of this volume are defined by the edges of the image. The near face of this volume is the lower end of the redshift bin in question. The far face of the volume is either the upper end of the redshift bin or $z_{\rm lim}$, the redshift at which the object would be fainter than the limiting magnitude of the sample, whichever is smaller. The limiting redshift, $z_{\rm lim}$, is found by artificially moving the object out in redshift and recalculating its apparent magnitude, taking into account the change in distance modulus and the k-corrections, until it reaches the magnitude limit of the survey, in this case $H_{\rm AB} = 26.5$ mag. The k-corrections were computed by interpolation using the best-fitting template from the photometric redshift procedure. The next step is to bin the galaxies by mass and sum over the galaxies in each bin, weighting by $1/V_a$. The mass functions are shown in Figure 2.

The top row of panels in Figure 2 shows the mass functions, $\Phi(M)$, for four redshift slices. The bottom row of panels shows the mass density functions, $M\Phi(M)$. Integrating over $M\Phi(M)$ gives the total stellar mass density. The bottom row of panels show that while we have fairly good coverage on the parts of the mass function that contribute most to the total mass, we do not cover the full range necessary. To extrapolate beyond the observed range, we fit Schechter (1976) functions to the data points:

$$\Phi(M)dM = \Phi^*(M/M^*)^\alpha\ \exp\left(-M/M^*\right)d(M/M^*), \tag{4}$$

where Φ^* is the overall normalization, α is the faint end slope, and M^* is the characteristic mass. These fits are shown by the lines in Figure 2. The fits are well constrained around M^*, well constrained at lower masses (with the possible exception of the $3 < z < 6$ redshift bin), and mostly well constrained at the high-mass end, with the notable exception of the $2 < z < 3$ redshift bin.

To obtain the total mass density, one must integrate the mass density function. This has the analytic form

$$M_{\rm tot} = \int_0^\infty M\Phi(M)\,dM = M^*\Phi^*\Gamma(\alpha+2), \tag{5}$$

where Γ is the gamma function. The results of this integration for the four redshift bins are shown as filled points in the top panel of Figure 3.

3.4. *Total Mass Uncertainties*

Before turning to a discussion of Figure 3 it is necessary to describe the possible uncertainties associated with our measurements. Besides the usual Poisson noise, there are three sources of uncertainty. Instead of spectroscopic redshifts, we use photometric redshifts, which have significantly larger associated errors. This can shift galaxies out of the correct redshift bin, affect their V_a weighting, and change the measured mass of the galaxy. Next, there is some uncertainty associated with the mass measurement itself, as discussed in § 3.2. Finally, the coverage of the mass density function is not perfect, which means that the Schechter fitting described in § 3.3 may be insufficiently constrained.

[7] See http://orca.phys.uvic.ca/~gwyn/MMM/nicmos.html.

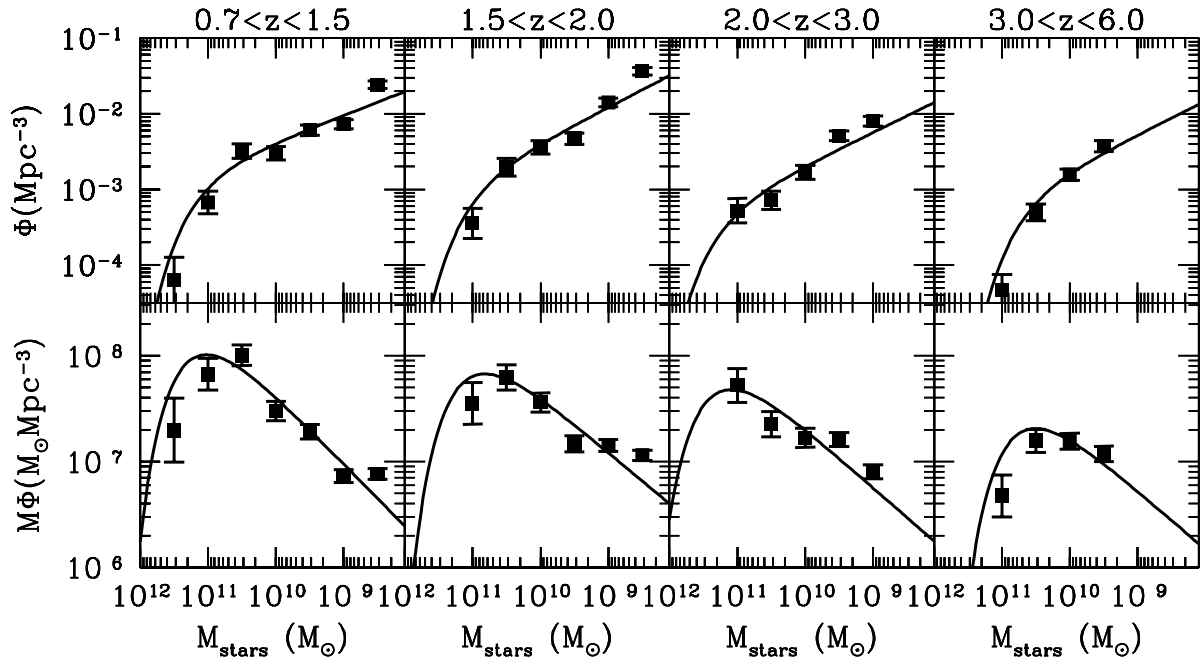

FIG. 2.—Mass functions. The top four panels show the mass functions for the indicated redshift ranges. The bottom four panels show the mass functions from the top panels multiplied by mass to give the mass density functions. The lines are Schechter (1976) function fits to the data. Eddington (1913) corrections have been applied to the data. The error bars indicate Poisson errors only.

Furthermore, when one measures the distribution of a parameter with a nonnegligible associated error, systematic effects will be noted, as first discussed by Eddington (1913). Even if the error bars are symmetric, more low-mass objects will scatter into the high-mass bins than high-mass objects will scatter into the low-mass bins, simply because there are more low-mass objects to be scattered. This systematic effect can be corrected if one has a good understanding of the error.

To investigate the uncertainties and to make the Eddington corrections, we used a Monte Carlo technique. To the original catalog of galaxies we added noise to the measured redshifts [$\sigma_z = 0.06(1+z)$] and masses ($\sigma_{\rm mass} = 0.1$ for $H_{\rm AB} < 25$ mag and $\sigma_{\rm mass} = 0.2$ for $H_{\rm AB} > 25$ mag). Further, we simulated the effects of redshift error on the derived masses by noting the relative shift in luminosity distance caused by the redshift error and applying the same shift to the mass. From these "noisy" catalogs we derived mass functions, integrated over fitted Schechter functions, and computed total stellar masses. The rms of the range of total stellar masses derived after 100 actualizations was used for the error bars in Figure 3. The Eddington corrections thus calculated were applied to the points. They were found to be negligible except for the highest mass bin, for which they were on the order of 0.2 dex. The Eddington corrections adjust the final masses by about 15%.

4. DISCUSSION

4.1. *The Evolution of the GSMD*

Figure 3 shows the buildup of stars in galaxies as a function of time. The top panel shows the GSMD, while the bottom panel shows the star formation rate. The top panel can be thought of as $M_*(t)$, while the bottom panel can be thought of as its derivative, $dM_*(t)/dt$. This panel is the reverse of the Lilly-Madau diagram, with cosmic time instead of redshift on the horizontal axis. The bottom panel shows a number of measurements of the star formation rate from the literature (Treyer et al. 1998; Hughes et al. 1998; Gwyn 2001; Flores et al. 1999; Steidel et al. 1999; Wilson et al. 2002; Giavalisco et al. 2004). All the star formation rate data shown in Figure 3 have been corrected for extinction by the authors of the individual papers. The only exception is the Bouwens et al. (2004b) data, which necessitated an extinction correction of 0.8 dex in order to bring this data onto the same system as the other data. Where appropriate, we have also applied incompleteness corrections assuming a Schechter extrapolation with $\alpha = -1.5$. For example, Bouwens et al. (2004b) only compute the UV luminosity function down to $L = 0.3L_*$. Extrapolating over the full range of L implies a correction of 0.36 dex.

The top panel of Figure 3 shows our measurements of the global mass density as solid points, together with a number of measurements from the literature (Rudnick et al. 2003; Dickinson et al. 2003; Fontana et al. 2004; Drory et al. 2004, 2005) as assorted open points. The authors of the above works have corrected their data for the unobserved portion of the mass function. In their analysis of the GDDS, Glazebrook et al. (2004) have chosen not to extrapolate beyond what they observe. The GDDS data for galaxies more massive than $\log(M/M_\odot) > 10.2$ are plotted as lower limits. The corrections for the choice of IMF, discussed in § 3.2, have been applied.

The solid lines in both panels of Figure 3 come from Hartwick (2004), who derived the global star formation history from observations of the local universe. Briefly, the model uses the distribution in metallicity of stars to derive dM_*/dZ (where Z is the metallicity) and the age-metallicity relationship for globular clusters to derive dZ/dt (where t is the age of the universe). Combining dM_*/dZ and dZ/dt, one obtains $dM_*/dt \equiv$ SFR, the star formation rate. This simple model does a very good job of explaining the star formation history of the universe, as shown by the agreement between it and the observations in the bottom panel. Using this star formation history as an input to the PEGASE 2.0 software, we compute a model GSMD. The result is plotted in the top panel. It is in excellent agreement with our GSMD measurements. Note that this agreement is not dependent

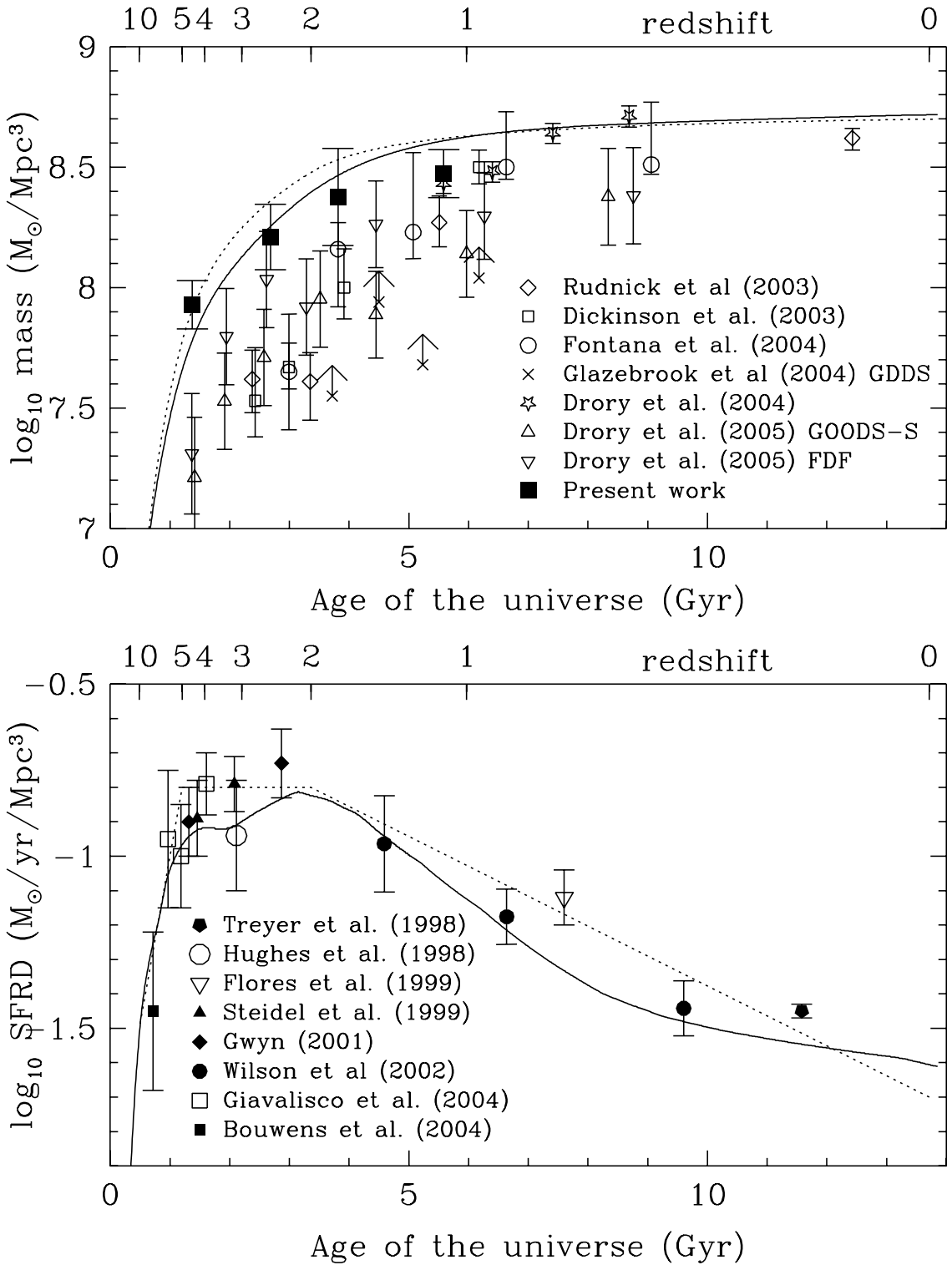

FIG. 3.—Stellar mass evolution. The bottom panel shows the star formation rate history of the universe. The points indicate measurements of the SFRD from the literature. The top panel shows the stellar mass evolution from this work along with data from the literature. The GDDS points are shown as lower limits. In both panels, the solid line shows the model of Hartwick (2004). The dotted line is an arbitrary parameterization of the star formation rate history (not a model) in the bottom panel and the integral of this parameterization in the top panel. See the text for references.

on the details of the Hartwick model. Almost any description of the star formation history that agrees with the observed star formation rates will, once integrated, produce good agreement with GSMD. This is illustrated by the dotted lines in Figure 3. In the bottom panel, this shows an arbitrary, three-segment "connect-the-dots" description of the star formation history. The three segments represent the rise of the star formation rate at $z < 2$, a plateau at $2 > z < 5$, and the falloff at $z > 5$. A two-segment description (rising to $z = 2$ and falling thereafter) going through the measured points produces similar results. In the top panel the dotted line shows the results of integrating (again with PEGASE 2.0) this star formation history. Again, there is good agreement with our GSMD calculations.

Note that converting a star formation rate to GSMD is a fairly robust procedure. It is fairly insensitive to the details of the population modelling. Indeed, there is only a slight loss of accuracy even if one makes the extreme assumption that all stars, once created, never die. This is because (for all reasonable IMFs) the bulk of the mass in stars comes from stars of less than 1 $M_{\odot}$, which have a main-sequence lifetime of approximately a Hubble time. In this simplified case one can do a straight integration of the dM_*/dt (with $M_* = 0$ at $t = 0$) to determine $M(t)$.

4.2. *Comparison with Previous Work*

There are two things to note in the top panel of Figure 3. The first is the excellent consistency between our measurements of GSMD and the integral of the star formation rate. The other is the disagreement between our measurements and those of previous researchers. The error bars of some authors overlap with ours, but on the whole there remains a systematic offset. This may be merely because the NICMOS UDF data probe slightly farther along the mass functions than other data sets, reducing the amount of extrapolation required at the low-mass end. However, we also use slightly different procedures than other authors, which may also cause the offset. We explored several possible causes.

We use a Kroupa IMF, whereas most authors use the Salpeter (1955) IMF. However, the offset of Figure 3 cannot be entirely due to our choice of IMF. Even if the IMF offsets discussed in § 3.2 are not applied, there is still a significant difference.

We use PEGASE (Fioc & Rocca-Volmerange 1997) stellar population models rather than the Bruzual & Charlot (2003) models used by other authors. To check that this is not a source of systematic error, the template fitting described in § 3.1 was redone using the Bruzual & Charlot templates. While there were differences in the derived masses, they were not systematic. The scatter between the PEGASE masses and the Bruzual & Charlot masses was typically 0.15 dex for a given galaxy, no greater than the internal uncertainties discussed in § 3.2.

Another procedural difference between us and some other authors is that we compute masses for each galaxy and integrate over the resulting mass functions. Some authors (Dickinson et al. 2003; Rudnick et al. 2003) integrate instead the galaxy luminosity function and multiply the resulting total luminosity by an average mass-to-light ratio. This has the advantage of masking any transient events that can temporarily alter the mass-to-light ratio of a given galaxy. The disadvantage is that the relatively simple star formation histories of individual galaxies (e.g., a single burst for a typical elliptical galaxy, continuous formation for a disk galaxy) are merged, producing a more complex star formation history. Rudnick et al. (2003) showed that integrating over the mass instead of integrating over the luminosity might in extreme cases cause a systematic shift of 0.25 dex. However, this can only explain the difference between our work and some authors (Dickinson et al. 2003; Rudnick et al. 2003), since the other authors used a similar method to ours.

Two other possible sources of error are the effect of extinction and the details of the extrapolation to the faint end of the mass function. Possible errors in extinction correction for each galaxy is effectively included in the mass uncertainties discussed in § 3.2. The extrapolation uncertainties are folded into the error bars on the points in the top panel of Figure 3 via the Monte Carlo method described in § 3.4.

It is possible that the cumulative effect of all these variations in procedure causes the difference between our measurements and previous work. The difference is not very large; our error bars overlap with those of several authors. However, we cannot point out one particular procedural difference that would cause a systematic shift without taking the data of another author, running it through our machinery, and comparing the results at each step with those from the other author's machinery. Since this is impractical, we have taken the approach of documenting our procedures in detail so that readers can see which procedural choices we made.

If the other authors are correct, then we need an explanation for the difference between their measurements of the GSMD and the integral of the SFRD. A number of possibilities have been suggested. For example, one explanation is a change in the average extinction in galaxies over time; i.e., galaxies have lower extinction at high redshift than is currently thought. If this were the case, the extinction correction would be smaller, and the deduced star formation rate would be lower at high redshift. Less star formation at high redshift means less mass buildup. Alternatively, the IMF might vary with redshift in such a way as to reconcile the GSMD and the SFRD. However, if our measurements are correct, no explanation is required.

4.3. *The Epoch of Galaxy Formation*

From Figure 3, we can set limits on the amount of star formation that went on before $z = 4.5$, our highest redshift point. For the concordance cosmology, $z = 4.5$ corresponds to a cosmic age of $t = 1.37$ Gyr. We find that the mass in stars at this point was $8.63 \times 10^7\ M_{\odot}\ \mathrm{Mpc}^{-3}$. If the epoch of galaxy formation lies at $t = 0$, then the average SFRD at $z < 4.5$ must have been close to $8.63 \times 10^7\ M_{\odot}\ \mathrm{Mpc}^{-3}/1.37\ \mathrm{Gyr} = 0.063\ M_{\odot}\ \mathrm{yr}^{-1}\ \mathrm{Mpc}^{-3}$. This is in good agreement with the results of Bouwens et al. (2004b). If, on the other hand, the epoch of galaxy formation was at $z = 10$ or 6, the same mass of stars must have been formed in only 0.9 or 0.4 Gyr, respectively. Then the corresponding star formation rates must be 0.097 or 0.21 $M_{\odot}\ \mathrm{yr}^{-1}\ \mathrm{Mpc}^{-3}$. The $z = 6$ figure represents a very significant SFRD, greater than the currently measured peak of the SFRD at $z = 2.5$ and completely incompatible with the measurements of Bouwens et al. (2004b). Turning the problem around, if we assume the *maximum* star formation rate allowed by the error bars on Bouwens et al. (2004b) at $z = 7$ and the *minimum* mass allowed by our highest redshift data point, we compute the *latest* possible epoch of galaxy formation to be $z = 16$.

5. SUMMARY

We have measured the buildup of the stellar mass of galaxies from $z \sim 6$ to $z \sim 1$. Our measurements are consistent with the predictions from star formation rate density (SFRD). The derived evolution of the global stellar mass density (GSMD) of galaxies is consistent with previous SFRD measurements over

the observed range of redshifts. Our measurements of the GSMD show an offset with respect to previous measurements of the GSMD. If we are to maintain consistency between the global stellar mass and the observed star formation rate, the epoch of galaxy formation must be at least $z = 16$.

F. D. A. H. gratefully acknowledges financial support from a discovery grant from NSERC. S. D. J. G. was supported partially from the above grant and from an NSERC CRO grant, which supports Canadian participation in the CFHT Legacy Survey.

REFERENCES

Abraham, R. G., et al. 2004, AJ, 127, 2455
Arnouts, S., et al. 2001, A&A, 379, 740
Baldry, I. K., & Glazebrook, K. 2003, ApJ, 593, 258
Benítez, N. 2000, ApJ, 536, 571
Bertin, E., & Arnouts, S. 1996, A&AS, 117, 393
Bouwens, R. J., et al. 2004a, ApJ, 606, L25
———. 2004b, ApJ, 616, L79
Bruzual, G., & Charlot, S. 2003, MNRAS, 344, 1000
Bunker, A. J., Stanway, E. R., Ellis, R. S., & McMahon, R. G. 2004, MNRAS, 355, 374
Calzetti, D. 1997, in AIP Conf. Proc. 408, The Ultraviolet Universe at Low and High Redshift: Probing the Progress of Galaxy Evolution (New York: AIP), 403
Coleman, G. D., Wu, C.-C., & Weedman, D. W. 1980, ApJS, 43, 393
Croom, S. M., Warren, S. J., & Glazebrook, K. 2001, MNRAS, 328, 150
Dickinson, M., Papovich, C., Ferguson, H. C., & Budavári, T. 2003, ApJ, 587, 25
Drory, N., Bender, R., Feulner, G., Hopp, U., Maraston, C., Snigula, J., & Hill, G. J. 2004, ApJ, 608, 742
Drory, N., Feulner, G., Bender, R., Botzler, C. S., Hopp, U., Maraston, C., Mendes de Oliveira, C., & Snigula, J. 2001, MNRAS, 325, 550
Drory, N., Salvato, M., Gabasch, A., Bender, R., Hopp, U., Feulner, G., & Pannella, M. 2005, ApJ, 619, L131
Eddington, A. S. 1913, MNRAS, 73, 359
Fioc, M., & Rocca-Volmerange, B. 1997, A&A, 326, 950
Flores, H., et al. 1999, ApJ, 517, 148
Fontana, A., et al. 2004, A&A, 424, 23
Fruchter, A. S., & Hook, R. N. 2002, PASP, 114, 144
Giavalisco, M., et al. 2004, ApJ, 600, L103
Glazebrook, K., et al. 2004, Nature, 430, 181
Gwyn, S. D. J. 2001, Ph.D. thesis, Univ. Victoria
Hartwick, F. D. A. 2004, ApJ, 603, 108
Heidt, J., et al. 2003, A&A, 398, 49
Hughes, D. H., et al. 1998, Nature, 394, 241
Kinney, A. L., Calzetti, D., Bohlin, R. C., McQuade, K., Storchi-Bergmann, T., & Schmidt, H. R. 1996, ApJ, 467, 38
Kron, R. 1980, ApJS, 43, 305
Kroupa, P., Tout, C. A., & Gilmore, G. 1993, MNRAS, 262, 545
Labbé, I., et al. 2003, AJ, 125, 1107
Le Fèvre, O., et al. 2004, A&A, 428, 1043
Lilly, S. J., Fèvre, O. L., Hammer, F., & Crampton, D. 1996, ApJ, 460, L1
Loh, E. D., & Spillar, E. J. 1986, ApJ, 303, 154
Madau, P. 1995, ApJ, 441, 18
Madau, P., Ferguson, H. C., Dickinson, M. E., Giavalisco, M., Steidel, C. C., & Fruchter, A. S. 1996, MNRAS, 283, 1388
Madau, P., Pozzetti, L., & Dickinson, M. 1998, ApJ, 498, 106
Oke, J. B. 1974, ApJS, 27, 21
Rettura, A. 2004, ESO/GOODS-CDFS Spectroscopy Master Catalogue (Garching: ESO), http://www.eso.org/science/goods/spectroscopy/CDFS_Mastercat/
Rudnick, G., et al. 2003, ApJ, 599, 847
Salpeter, E. E. 1955, ApJ, 121, 161
Schechter, P. 1976, ApJ, 203, 297
Stanway, E. R., et al. 2004, ApJ, 604, L13
Steidel, C. C., Adelberger, K. L., Giavalisco, M., Dickinson, M., & Pettini, M. 1999, ApJ, 519, 1
Strolger, L., et al. 2004, ApJ, 613, 200
Szokoly, G. P., et al. 2004, ApJS, 155, 271
Treyer, M. A., Ellis, R. S., Milliard, B., Donas, J., & Bridges, T. J. 1998, MNRAS, 300, 303
Vanzella, E., et al. 2005, A&A, 434, 53
Wilson, G., Cowie, L. L., Barger, A. J., & Burke, D. J. 2002, AJ, 124, 1258